Amorphous hetero-structure iron/cobalt oxyhydroxide with atomic dispersed palladium for oxygen evolution reaction

Shuai Yang [a], Lu Lu [b], Peng Zhan [a], Zhihao Si [a], Leyi Chen [a], Yan Zhuang [a], Peiyong Qin [a,b,*]

[a] National Energy R&D Center for Biorefinery, Beijing University of Chemical Technology, Beijing 100029, China
[b] Paris Curie Engineer School, Beijing University of Chemical Technology, Beijing 100029, China

ARTICLE INFO

ABSTRACT

The activity of iron oxyhydroxides (FeOOH) in oxygen evolution reaction (OER) is limited by their poor conductivity and the high energy barrier in the rate-determining step. Herein, we report the immobilization of atomic dispersed Pd species on Co doped FeOOH, realizing the preparation of amorphous hetero-structure $FeCo_aOOH-Pd_b$. In the case of Co/Fe of 0.68 and Pd/Fe of 0.026, the coexisting structure of nanorods and nanospheres with appropriate oxygen vacancies and unsaturated active centers increases the number of active sites and enhances the intrinsic activity of the electrocatalyst. The density functional theory results uncover that the $FeCo_{0.68}OOH-Pd_{0.026}$ optimizes the binding energies of *O and *OOH, and accelerates the OER kinetics. The rationally designed $FeCo_{0.68}OOH-Pd_{0.026}$ exhibits excellent OER activity and reliability, manifesting a Tafel slope of $37.5 \, mV \, dec^{-1}$, a low overpotential of $265.1 \, mV$ at $10 \, mA \, cm^{-2}$, which has the potential to realize the large-scale implementation of water splitting.

1. Introduction

Nowadays, with the consideration of energy crisis and environmental pollutant, it is urgent to exploit and utilize new energy sources. Water splitting into hydrogen is a promising strategy for renewable energy storage and eco-friendly energy source production owing to its advantage of large-scale production feasibility [1–4]. Oxygen evolution reaction (OER) ($4OH^- \rightarrow O_2 + 2\,H_2O + 4e^-$ in alkaline; $2\,H_2O \rightarrow O_2 + 4\,H^+ + 4e^-$ in acidic), as a half reaction, plays a critical role in the water splitting, but its slow kinetics results in high overpotential, which seriously hinders the efficiency of energy conversion [5,6]. At present, iridium oxide (IrO_2) and ruthenium oxide (RuO_2) have been proven to exhibit best performance in the OER [7–10]. However, the scarcity and high price of Ir and Ru as noble metals limit their potential for large-scale applications [11,12]. In order to utilize the earth-abundant and non-noble resources, various materials with low cost and low OER overpotential such as oxy(hydroxides) [13,14], transition-metal oxides [15,16], nitrides [17,18], sulfides [19,20], and phosphides [21,22] have been widely developed and applied. Notably, cost-efficient and non-toxic iron oxyhydroxides (FeOOH) have become one of the most promising OER catalysts due to their advanced electrochemical performance in alkaline solutions [23,24]. However, high

energy barrier during the conversion of M-O to M-OOH and poor electrical conductivity are key issues that limit the enhancement of FeOOH activity [25,26]. Therefore, it is urgent to improve the electronic conductivity of FeOOH and optimize the binging energies of intermediates (*OH→*O→*OOH→*O$_2$) in OER pathway to overcome the sluggish kinetics of water splitting.

Heteroatomic doping is a vital method in catalyst design for modulating morphology, enhancing electrical conductivity, and optimizing electronic structure for host materials [27,28]. Cobalt (Co) and nickel (Ni) are widely used doping elements in cocatalysts with FeOOH [29, 30]. Particularly, owing to the favorable charge transfer ability and lower overpotential of CoOOH containing redox couple (Co^{2+}/Co^{3+}), Co is the more suitable doping element for accelerating the OER processes of FeOOH [31,32]. However, in the reported works, the FeCoOOH catalysts formed by Co doping in FeOOH are mostly crystalline rather than amorphous, which result in the catalysts lacking the advantages of amorphous materials with abundant coordinately unsaturated atoms and rich defects [33,34]. Additionally, disordered long-range atomic arrangement and flexible structure in amorphous materials are conducive to precise control of atomic ratio and rapid charge conduction, which are of positive significance for facilitating kinetics and exploring reaction mechanisms [35,36]. Thus, constructing amorphous FeCoOOH

---

by Co doping is a feasible approach to overcome the insufficient electronic conductivity of FeOOH and regulate the electronic structure of the electrocatalysts.

In order to enhance the intrinsic activity of OER, according to Sabatier's theory, the adsorption energy between the surface of the catalysts and the intermediate cannot be too strong or too weak [37]. At present, the generations of oxygen vacancies and atomic dispersion level active centers are recognized strategies to avoid scaling relationship in OER processes [38,39]. By changing the conductivity of bulk and modulating the molecular adsorption properties of surface, it has been demonstrated that an appropriate amount of oxygen vacancies indeed plays a positive role in improving OER activity [40–43]. Besides, as the size of the active sites of noble metal decreases, the electrocatalytic performance is significantly improved, while minimizing the content of noble metal and saving the cost of the catalysts [44]. Compared with Pd nanoparticles, atomic dispersed Pd species maximize the number of active sites and form unsaturated coordination environments, increasing the electrochemical surface area while optimizing the electronic structure [45,46] As a consequence, using Co atoms doping to regulate the concentration of oxygen vacancies and utilizing the immobilization of atomic dispersed Pd species are promising strategies to increase the quantity of active sites and reduce the Gibbs free energy barrier between M-O and M-OOH.

Herein, amorphous hetero-structure $FeCo_{0.68}OOH\text{-}Pd_{0.026}$ was prepared by doping an appropriate amount Co element and immobilizing atomic dispersed Pd species in FeOOH as an efficient OER electrocatalyst. The amorphous structures achieve different proportions of Co doping and morphology changes from nanowire to ideal heterostructure to nanospheres. The doping of Co enhances electron transfer ability and increases the concentration of oxygen vacancies that modulate the electronic structure. Compared with Pd nanoparticles, atomic dispersed Pd species provide a large quantity of active sites and enhance the intrinsic activity of the electrocatalyst. Moreover, density functional theory (DFT) calculations reveal that due to the redistribution of charge, the adsorption of intermediates in the OER processes is optimized, and the energy barrier of the rate-determining step (RDS) is significantly reduced. $FeCo_{0.68}OOH\text{-}Pd_{0.026}$ overcomes the low electronic conductivity and sluggish kinetics in OER of FeOOH, exhibiting an overpotential of 265.1 mV at 10 mA cm^{-2} and a Tafel slope of 37.5 mV dec^{-1} which is one of the most excellent performances in the Fe/Co-based OER electrocatalysts.

2. Experimental section

2.1. Materials

Iron (III) acetylacetonate (Fe(acac)$_3$), cobalt (III) acetylacetonate (Co(acac)$_3$), palladium (II) acetylacetonate (Pd(acac)$_2$), cobalt tetracarbonyl dime (Co$_2$(CO)$_8$), ethylene glycol, potassium hydroxide (KOH), ethanol, acetone, commercial RuO$_2$ and Pt/C were provided by Shanghai Macklin Biochemical Co., Ltd. The Suzhou Sinero Technology Co., Ltd supplied carbon paper (TGP-H-060) from Toray, anion exchange membrane (Sustainion X37–50) from Dioxide Materials, and Nafion D520 (5%) from Dupont. Except for carbon paper that needs to be pre-treated with deionized water and acetone, all other materials were directly used after purchase.

2.2. Preparation of $FeCo_aOOH\text{-}Pd_b$

In a typical synthesis, m g Fe(acac)$_3$, n g Co(acac)$_3$, o g Pd(acac)$_2$, and 0.15 g Co$_2$(CO)$_8$ were added into 20 mL ethylene glycol, followed by magnetic stirring at room temperature for 1 h. The obtained homogeneous solution was transferred to a Teflon-lined stainless-steel autoclave and treated at 125 °C for 48 h. Then, the solution was cooled down to room temperature and centrifuged to obtain the product. The product was washed with ethanol and acetone for several times. The final

product was obtained by drying overnight in a vacuum at 70 °C. The values of a and b were determined by Co:Fe (mol%) and Pd:Fe (mol%) in the inductively coupled plasma optical emission spectrometer (ICP-OES) results.

In the preparation of $FeCo_{0.25}OOH\text{-}Pd_x$, $FeCo_{0.37}OOH\text{-}Pd_x$, $FeCo_{0.68}OOH\text{-}Pd_x$, $FeCo_{0.83}OOH\text{-}Pd_x$, and $FeCo_{1.01}OOH\text{-}Pd_x$, m=1.1/0.9/0.8/0.7/0.5, n=0/0.2/0.3/0.4/0.6, o=0.02, respectively. The Pd$_x$ indicates that the molar content of Pd in each sample is consistent.

In the preparation of $FeCo_{0.68}OOH$, $FeCo_{0.68}OOH\text{-}Pd_{0.012}$, $FeCo_{0.68}OOH\text{-}Pd_{0.026}$, $FeCo_{0.68}OOH\text{-}Pd_{0.051}$ and $FeCo_{0.68}OOH\text{-}Pd_{0.072}$, m=0.8, n=0.3, o=0/0.01/0.02/0.04/0.06, respectively.

2.3. Material characterization

Transmission electron microscopy (TEM), high-resolution TEM (HR-TEM), high-angle annular dark field-scanning TEM (HAADF-STEM), and energy dispersive X-ray spectroscopy (EDS) images were captured by using a Tecnai G2 F30 S-TWIN operated at 300 kV through dropping the catalysts on Cu grids. Agilent ICPOES730 was used to measure the relative content of Fe, Co, and Pd in $FeCo_aOOH\text{-}Pd_b$. An X-ray diffractometer named Bruker D8 Advance was used to obtain X-ray diffraction (XRD) patterns of the catalysts under Cu Kα radiation at a λ of 1.54184 Å. The Thermo Scientific Nicolet IS20 spectrometer was used for Fourier transformation infrared spectroscopy (FT-IR) characterization, with a measurement range of 4000–400 cm^{-1}. The Thermo Scientific Escalab Xi+ spectrometer was used for recording X-Ray photoelectron spectroscopy (XPS) data. The EG&G ORTEC fast-fast coincident system was used to analyze the positron annihilation lifetime spectroscopy (PALS) of $FeCo_aOOH\text{-}Pd_x$. Positron source (^{22}Na) sandwiched between sample pieces, and the resolution of spectrometer was 210 ps. Each spectrum contains 2×10^6 data points, which were deconvoluted into three different lifetime components through LT-9.

2.4. Electrochemical measurements

An airtight H-type cell with a CHI660E workstation (Shanghai CH Instruments Co., China) was used for electrochemical measurements. An anion exchange membrane separated the cathode chamber from the anode chamber. The platinum gauze was placed in the cathode chamber as the counter electrode, and the reference electrode Ag/AgCl (3 M KCl aqueous solution) electrode was placed together with the working electrode in the anode chamber. The reference Ag/AgCl was calibrated versus reversible hydrogen electrode (RHE) as follow (Eq. 1):
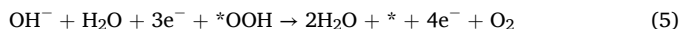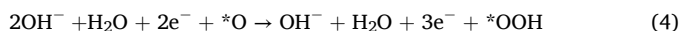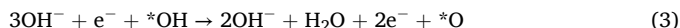
$$E \text{ (vs RHE)} = E \text{ (vs Ag/AgCl)} + 0.0591 \times pH + 0.210 \text{ V} \qquad (1)$$

To prepare the working electrode, 1 mg catalyst, 1 mL acetone, and 20 μL Nafion D520 were mixed and treated by sonicating for 1 h to obtain a homogeneous ink. 200 μL of the catalyst ink was dropped onto the carbon paper (0.5 cm^{-2}) and dried 30 min in a vacuum. The OER polarization curves were conducted in O$_2$-saturated 1.0 M KOH with a scan rate of 5 mV s^{-1} and corrected by iR compensation. Before the test, the working electrode was repeatedly cyclic voltammetry tests in the electrolyte to stabilize the current. Tafel plots were used to calculate the Tafel slopes (b) by fitting the overpotential (η) and current density (j) in the Tafel equation (η=blog(j)+a). Electrical impedance spectroscopy (EIS) tests were performed under open circuit voltages, with an amplitude of 5 mV and a testing range of 100000–0.01 Hz. Cyclic voltammetry (CV) was carried out with different scan rates to estimate the electrochemical double layer capacitance (C$_{dl}$). The potential intervals of CV were in the non-Faradaic region centered on the open circuit potential. The scan rates were increased from 20 mV s^{-1} to 180 mV s^{-1}. The C$_{dl}$ was calculated by plotting the Δj against the scan rate.

2.5. Theoretical calculations

The DFT calculations were conducted by utilizing CP2K packages [47]. The pseudopotentials used was Goedecker–Teter–Hutter [48]. The basis set was a hybrid Gaussian (DZVP)-plane wave, and the cutoff was 400 Ry [49]. The fitting of wave function relied on the auxiliary density matrix method. PBE0 was used to describe the system [50], and unrestricted Kohn-Sham DFT performed all calculations [51]. The simulations were carried out in a three-dimensional periodic boundary box of $11.628 \times 12.901 \times 20.853$ Å^3. In order to avoid interference between mirror images in the calculation results, a 15 Å vacuum region was created.

The OER occur via the following Eqs. (2–5):

$$4OH^- + * \rightarrow 3OH^- + e^- + *OH \tag{2}$$

$$3OH^- + e^- + *OH \rightarrow 2OH^- + H_2O + 2e^- + *O \tag{3}$$

$$2OH^- + H_2O + 2e^- + *O \rightarrow OH^- + H_2O + 3e^- + *OOH \tag{4}$$

$$OH^- + H_2O + 3e^- + *OOH \rightarrow 2H_2O + * + 4e^- + O_2 \tag{5}$$

The equation for calculating the reaction free energy (ΔG) for each step is as follow (Eq. 6):

$$\Delta G = \Delta E + \Delta ZPE - T\Delta S + \Delta G_U \tag{6}$$

where ΔE is the difference in total energy of the system before and after each reaction step, ΔZPE and ΔS are used to correct changes in zero-point energies and vibrational entropy during the OER processes, and $\Delta G_U = -eU$ (U=1.23 V).

3. Results and discussion

3.1. Synthesis and characterization of the FeCoOOH$_a$-Pd$_b$

The FeCo$_a$OOH-Pd$_b$ electrocatalysts were synthesized via a solvothermal method with Fe(acac)$_3$, Co(acac)$_3$, Pd(acac)$_2$, and Co$_2$(CO)$_8$ as precursors, and ethylene glycol as solvent at 125 °C. The molar ratios of Fe, Co, and Pd were determined by ICP-OES. Ethylene glycol is a key component that controls the formation of amorphous structure during the dissociation and condensation reactions by complexing with iron species [52,53]. FeCo$_a$OOH-Pd$_x$ with different Co/Fe ratios were prepared by adjusting the relative content of Fe(acac)$_3$ and Co(acac)$_3$, while their Pd atomic molar ratios (Pd/(Fe+Co)) were consistent (Table S1). FeCo$_{0.68}$OOH-Pd$_b$ catalysts with Co/Fe ratio of 0.68 but different Pd contents were achieved by changing the masses of Pd(acac)$_2$ in the precursors (Table S2).

The morphologies of prepared FeCo$_a$OOH-Pd$_x$ with different Co/Fe ratios were investigated by TEM. In the case of the lowest Co/Fe ratio (Fig. S1), the morphology of FeCo$_{0.25}$OOH-Pd$_x$ is a nanowire structure with a length over 1 μm and a diameter around 80 nm, the similar structures have been found in previous reports of FeOOH [54,55]. In Fig. S2, it can be observed that the morphology of the FeCo$_{0.37}$OOH-Pd$_x$ is a structure with a size of less than 500 nm in length and approximately 160 nm in diameter. Compared with FeCo$_{0.25}$OOH-Pd$_x$, the length of the nanostructure in FeCo$_{0.37}$OOH-Pd$_x$ decreases but the diameter increases, indicating a change in morphology from nanowire to nanorod due to the increase in Co/Fe ratio. As shown in Fig. 1a, at a Co/Fe ratio of 0.68, the morphology of FeCo$_{0.68}$OOH-Pd$_x$ (*viz* FeCo$_{0.68}$OOH-Pd$_{0.026}$) further develops into a hetero-structure of nanorods and nanospheres coexisting, and the nanospheres with a diameter concentrated around 47 nm

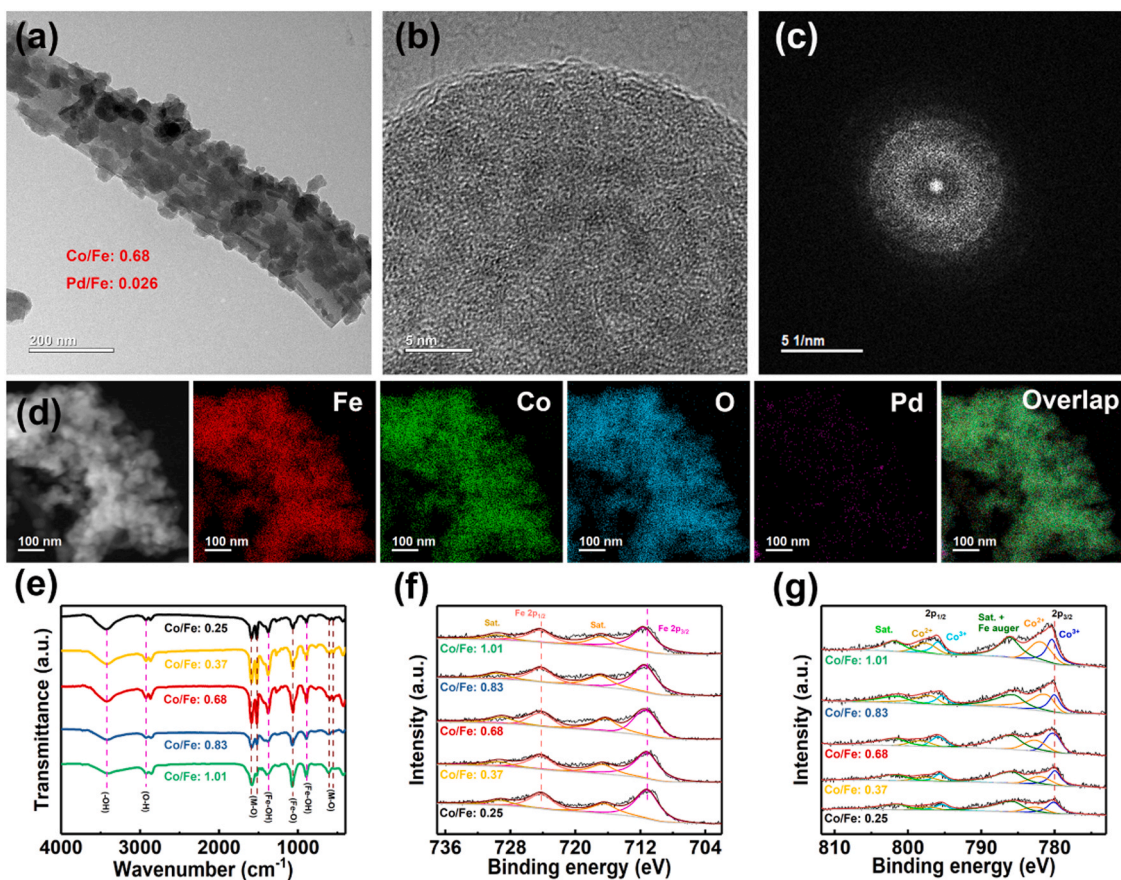**Fig. 1.** (a) TEM image, (b) HR-TEM image, (c) SAED pattern, and (d) TEM elemental mapping images of FeCo$_{0.68}$OOH-Pd$_{0.026}$. (e) FT-IR spectra of FeCo$_a$OOH-Pd$_x$. High-resolution XPS spectra of FeCo$_a$OOH-Pd$_x$: (f) Fe 2p and (g) Co 2p.

attached to the surface of the nanorods (Fig. S3). As the Co/Fe ratio further increases to 0.83, the nanorods completely disappear, and the $FeCo_{0.83}OOH-Pd_x$ is composed of uniform nanospheres with a diameter of 98 nm, as shown in Fig. S4. Fig. S5 reveals that in the $FeCo_{1.01}OOH-Pd_x$ with highest Co/Fe ratio, nanospheres cannot be observed and only irregular nanoparticles exist. The results of TEM indicate that Co doping has a significantly impact on the morphology of $FeCo_aOOH-Pd_x$, and a hetero-structure of nanospheres loaded on nanorods can be formed at a Co/Fe ratio of 0.68. The interconnection among FeO_6 octahedron, CoO_6 octahedron, and CoO_4 tetrahedron in $FeCo_aOOH-Pd_x$, fabricated by various sharing configurations, is the reason for the formation of amorphous structure [56]. Moreover, the increase of Co content leads to a higher proportion of CoO_4 tetrahedron, which affects the morphology of the $FeCo_aOOH-Pd_x$ [57].

HR-TEM was carried out to explore the detailed structures of the $FeCo_aOOH-Pd_x$. As shown in Fig. 1b, no clear crystal lattice fringes are observed in the $FeCo_{0.68}OOH-Pd_x$, and there are no strong diffraction rings in the corresponding selected area electron diffraction (SAED) pattern (Fig. 1c). The consistent results are shown in the $FeCo_{0.25}OOH-Pd_x$ (Fig. S1), $FeCo_{0.37}OOH-Pd_x$ (Fig. S2), $FeCo_{0.83}OOH-Pd_x$ (Fig. S4), and $FeCo_{1.01}OOH-Pd_x$ (Fig. S5), indicating the absence of crystals in the structures. In addition, the powder XRD patterns displayed in Fig. S6 show that no obvious characteristic diffraction peaks can be observed, which reflect that the addition of Pd with a low molar ratio and the value of Co/Fe ratio will not affect the amorphous structures of the $FeCo_aOOH-Pd_x$. The single elemental mapping images and overlapping image obtained by HAADF-STEM show that Fe, Co, O, and Pd atoms are homogenous distributed in $FeCo_{0.68}OOH-Pd_x$ (Fig. 1d), revealing uniform doping of Co element and no aggregation of Pd atoms.

The surface structure and composition of $FeCo_aOOH-Pd_x$ were investigated by FT-IR and XPS characterizations. The FT-IR spectra in the range of 4000–400 cm^{-1} are given in Fig. 1e. The broad band at 3424 cm^{-1} is attributed to the stretching vibration of the hydrogen bonded -OH [58], and the bands around 2924 cm^{-1} indicate the interaction between O-H band and nearby Co atoms [59]. The peaks at 1588, 1523, 598, and 552 cm^{-1} correspond to Co-O double bonds, Fe-O vibrational mode, Co-O^{2-} vibration, and Fe-O stretching vibration, respectively [60–62], and the corresponding peak intensities decrease with the decline of Fe content. The absorption bands at 1381 and 893 cm^{-1} could be assigned to Fe-OH vibrations, and peak at 1065 cm^{-1} could be attributed to Fe-O vibrations [63]. The full XPS spectra of the $FeCo_aOOH-Pd_x$ exhibit the peaks of Fe, Co, O, and Pd, confirming the high purity of $FeCo_aOOH-Pd_x$ (Fig. S7). From the high-resolution Fe 2p spectra of $FeCo_{0.68}OOH-Pd_x$ (Fig. 1f), two distinct peaks located at 711.4 and 724.3 eV are attributed to the spin-orbit couple of Fe $2p_{3/2}$ and Fe $2p_{1/2}$, corresponding to the Fe^{3+} oxidation state in FeOOH [64]. Furthermore, the two satellite peaks located at 716.3 and 729.1 eV are the features of FeOOH [65]. As the Co content increase, the characteristic peaks shift positively to higher binding energies, indicating the transfer of electrons from Fe to Co. For the high-resolution Co 2p spectra of $FeCo_{0.68}OOH-Pd_x$ (Fig. 1g), the two spin-orbit doublets at 780.6 and 796.1 eV are attributed Co $2p_{3/2}$ and Co $2p_{1/2}$, and the difference in binding energy values indicates the coexistence of Co^{3+} and Co^{2+} species [66]. As the proportion of Co atoms increases, the peak intensities of Co 2p enhance. The two satellite peaks at 785.9 and 801.7 eV can be attributed to the Co^{2+}, and the Fe auger peak around 784 eV increases the proportion of peak area at 785.9 eV [67]. The Co $2p_{3/2}$ peaks were deconvoluted into Co^{3+} (780.2 eV) and Co^{2+} (782.7 eV), as the Co/Fe ratio increases, the binding energy of Co 2p shifts towards Co^{2+}, and the proportion of peaks corresponding to Co^{3+} decreases, indicating an increase in the amount of Co^{2+}, which is related to an increase in the amount of oxygen vacancies [68]. Furthermore, variable metal valence can provide redox centers for electron hooping and donor-acceptor chemical adsorption sites, which play a positive role in improving conductivity and reversible adsorption of intermediates [69]. These spectroscopy characterizations confirm the formation of $FeCo_aOOH-Pd_x$,

reveal the modulation of Co doping on the surface composition and electronic structure of electrocatalysts.

XPS and PALS were performed to demonstrate the formation of oxygen vacancies in $FeCo_aOOH-Pd_x$. For the high-resolution O 1 s spectra shown in Fig. 2a, the peaks can be deconvoluted into four types at 530.3, 530.9, 531.5, and 532.3 eV, which are attributed to the metal-oxygen (M-O) bonds, metal-hydroxide (M-OH) structures, defect sites with low oxygen coordination, and surface-adsorbed H_2O molecules, respectively [69,70]. The higher Co/Fe ratio, the higher binding energy of O 1 s, and the larger area of the peak corresponding to oxygen vacancies, indicating a positive correlation between Co content and the number of oxygen vacancies. PALS is an established method for obtaining the size, type, and concentration of vacancies by measuring positron annihilation in low-density regions [71]. The PALS spectra of $FeCo_aOOH-Pd_x$ were fitted into three different lifetime components (Fig. S8). The shorter lifetime (τ_1) is attributed to the annihilation of positrons in monovacancies or oxygen vacancies, and the decrease in surrounding electron density leads to the increase in τ_1 [72]. The longer lifetime (τ_2) and longest lifetime (τ_3) are assigned to the annihilation of positrons in vacancy clusters with electron density lower than that of small-sized defects and nanoscale voids in materials respectively [73]. As shown in Fig. 2b, the τ_1 of $FeCo_{0.25}OOH-Pd_x$ is 0.136 ns, which is attributed to the inherent free positron lifetime. However, the τ_1 for $FeCo_{0.68}OOH-Pd_x$ is significantly longer at 0.198 ns, 45.6% greater than in $FeCo_{0.25}OOH-Pd_x$. Therefore, the prolonged τ_1 of $FeCo_{0.68}OOH-Pd_x$ reveals that a large number of oxygen vacancies were introduced into FeCoOOH by Co doping. Correspondingly, the relative intensity of τ_1 (I_1) is increased prominently, further demonstrating an increase in the number of oxygen vacancies (Fig. 2c). The higher the ratio of Co/Fe, the greater the τ_1 and I_1, indicating a positive correlation between the concentration of oxygen vacancies and the relative content of Co, reflecting the modulation of surface electronic structure by Co doping.

The influence of Pd molar ratio on the structure of $FeCo_{0.68}OOH-Pd_b$ was investigated. Consistent with the amorphous structure of $FeCo_{0.68}OOH-Pd_x$ with a Pd/Fe ratio of 0.026, no obvious lattice fringes were found in $FeCo_{0.68}OOH$ and $FeCo_{0.68}OOH-Pd_{0.012}$ (Fig. S9). As the HR-TEM image shown for $FeCo_{0.68}OOH-Pd_{0.051}$ in Fig. 3a, a triangular lattice fringes with a side length of 8.9 nm can be clearly observed on the surface of the amorphous support. The corresponding SAED pattern of $FeCo_{0.68}OOH-Pd_{0.051}$ and the lattice spacing of 0.223 nm indicate that the triangular nanostructure is composed of Pd (111) facet in a cubic phase, which is consistent with previous report [74]. In addition, EDS analysis also demonstrate that Pd is the constituent element of the triangular nanostructure with higher brightness in the HADDF-STEM image (Fig. S10). In the $FeCo_{0.68}OOH-Pd_{0.072}$ with highest Pd content (Fig. 3b), it can be observed that crystalline nanoparticles aggregate on the surface of the amorphous support, and the SAED pattern shows clear diffraction rings. In addition, Fig. 3c displays that in the XRD pattern of $FeCo_{0.68}OOH-Pd_{0.051}$ with a Pd/Fe ratio of 0.051, a characteristic peak at 40.1° indicates that Pd (111) is the dominant facet (JCPDS: 46–1043). In the XRD pattern of $FeCo_{0.68}OOH-Pd_{0.072}$, the diffraction peaks attributed to Pd is more distinct, indicating the aggregation of Pd atoms with larger molar ratio to form crystals. However, no obvious diffraction peaks were observed in $FeCo_{0.68}OOH-Pd_{0.012}$ and $FeCo_{0.68}OOH-Pd_{0.026}$. Combined with the results of HR-TEM and XRD, it can be inferred that Pd atoms in the $FeCo_{0.68}OOH-Pd_{0.026}$ are dispersed at atomic level. Moreover, the Pd species could be controlled from atomic dispersed species to nanoparticles by different loading contents of Pd, meaning that Pd species are immobilized on the $FeCo_{0.68}OOH$ surface. Oxygen vacancies and (oxo)hydroxyl group have strong interactions with metal atoms, which play a significant role in the stable binding of Pd species on the oxyhydroxide supports [75]. XPS was carried out to study the composition and valence state of Pd in $FeCo_{0.68}OOH-Pd_b$ (Fig. S11). For the high-resolution Pd 3d spectrum of $FeCo_{0.68}OOH-Pd_{0.026}$, the peaks located at 335.0 eV and 340.2 eV are assigned to the Pd $3d_{5/2}$ and Pd $3d_{3/2}$, corresponding to the Pd^0 species (Fig. 3d) [76]. Compared with
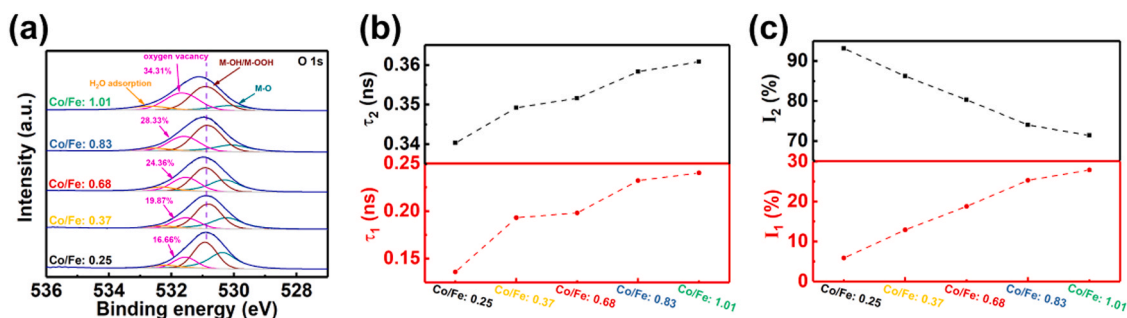
Fig. 2. (a) O 1 s high-resolution XPS spectra of $FeCo_aOOH-Pd_x$. (b) Positron lifetimes for different components and (c) their relative intensities of $FeCo_aOOH-Pd_x$.
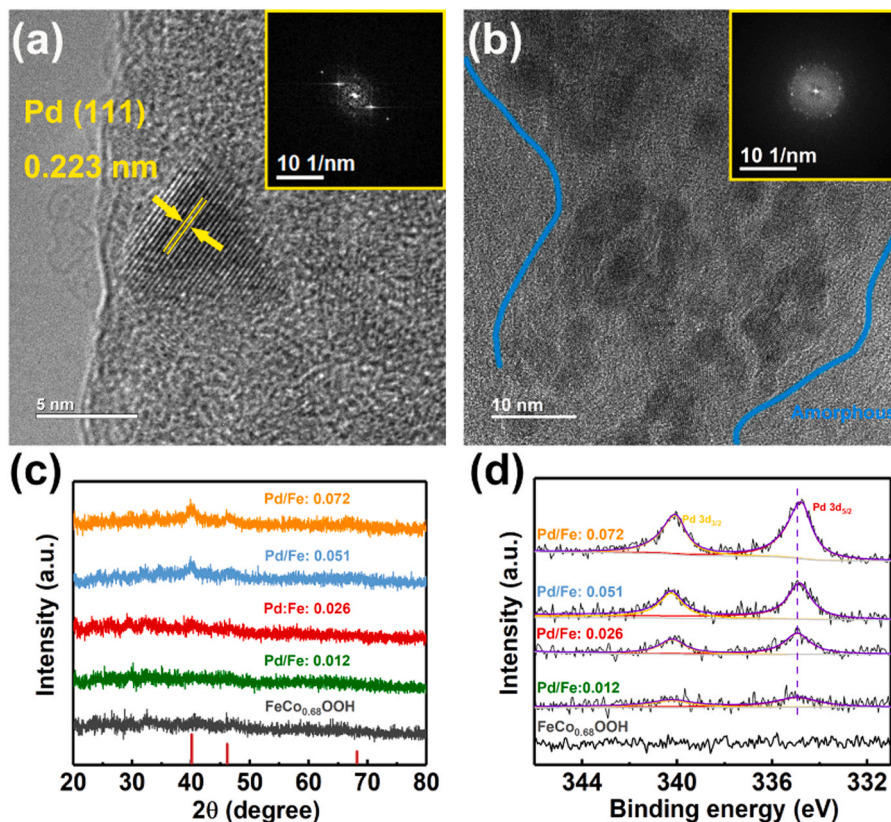

Fig. 3. HR-TEM images of (a) $FeCo_{0.68}OOH-Pd_{0.051}$ and (b) $FeCo_{0.68}OOH-Pd_{0.072}$, inset, the corresponding SAED patterns. (c) XRD patterns and (d) Pd 3d high-resolution XPS spectra of $FeCo_{0.68}OOH-Pd_b$.

$FeCo_{0.68}OOH-Pd_{0.026}$, a negative shift of 0.2 eV was found in $FeCo_{0.68}OOH-Pd_{0.072}$ (Pd $3d_{5/2}$, 334.8 eV), and the decrease in binding energy reveals charge transfer between Pd atoms and support, while the increase in Pd content weakens the interaction between Pd species and $FeCo_{0.68}OOH$ support.

3.2. Electrocatalytic property measurements

The OER performances of prepared $FeCo_aOOH-Pd_x$ were evaluated by using a conventional three-electrode cell in O_2-saturated 1 M KOH aqueous solutions. As the linear sweep voltammetry (LSV) curves shown in Fig. 4a, the onset potential of $FeCo_{0.68}OOH-Pd_x$ is 1.40 V vs RHE at 1 mA cm^{-2}, which is much lower than that of $FeCo_{0.25}OOH-Pd_x$ (1.51 V vs RHE at 1 mA cm^{-2}). Fig. 4b exhibits the relationship between overpotential and Co/Fe ratio. $FeCo_{0.25}OOH-Pd_x$ with the lowest Co/Fe ratio has the highest overpotential at 10 and 100 mA cm^{-2}, and when the Co/Fe ratio increases to 0.68, the overpotential of $FeCo_{0.68}OOH-Pd_x$ (265.1 mV at 10 mA cm^{-2} and 313.9 mV at 100 mA cm^{-2}) is the lowest.

After Co/Fe ratio reaches 0.68, increasing the proportion of Co has a negative impact on overpotential. Furthermore, the kinetics behaviors of $FeCo_aOOH-Pd_x$ electrocatalysts towards OER were investigated by Tafel plots (Fig. 4c). Consistent with the variation of overpotential with Co/Fe ratio, a smallest Tafel slope is found in $FeCo_{0.68}OOH-Pd_x$ (37.5 mV dec^{-1}), revealing the acceleration of OER kinetics by hetero-structure rich in oxygen vacancies. The five $FeCo_aOOH-Pd_x$ electrocatalysts follow the order $FeCo_{0.68}OOH-Pd_x$>$FeCo_{0.83}OOH-Pd_x$ >$FeCo_{0.37}OOH-Pd_x$>$FeCo_{1.01}OOH-Pd_x$>$FeCo_{0.25}OOH-Pd_x$, indicating that $FeCo_{0.68}OOH-Pd_x$ is the optimal electrocatalyst.

To unlock the derivation of the improved OER performances of $FeCo_{0.68}OOH-Pd_x$, EIS tests were performed. As shown in Fig. 4d, the charge-transfer resistance (R_{ct}) value of $FeCo_{0.68}OOH-Pd_x$ decreases dramatically compared to $FeCo_{0.25}OOH-Pd_x$, indicating that the sample with appropriate amount of Co doping has a relatively high carrier mobility across the Helmholtz layer, proving the change in charge state leads to lower internal resistance, resulting in faster electron transfer. Electrochemically active surface areas (ECSA) of $FeCo_aOOH-Pd_x$ were
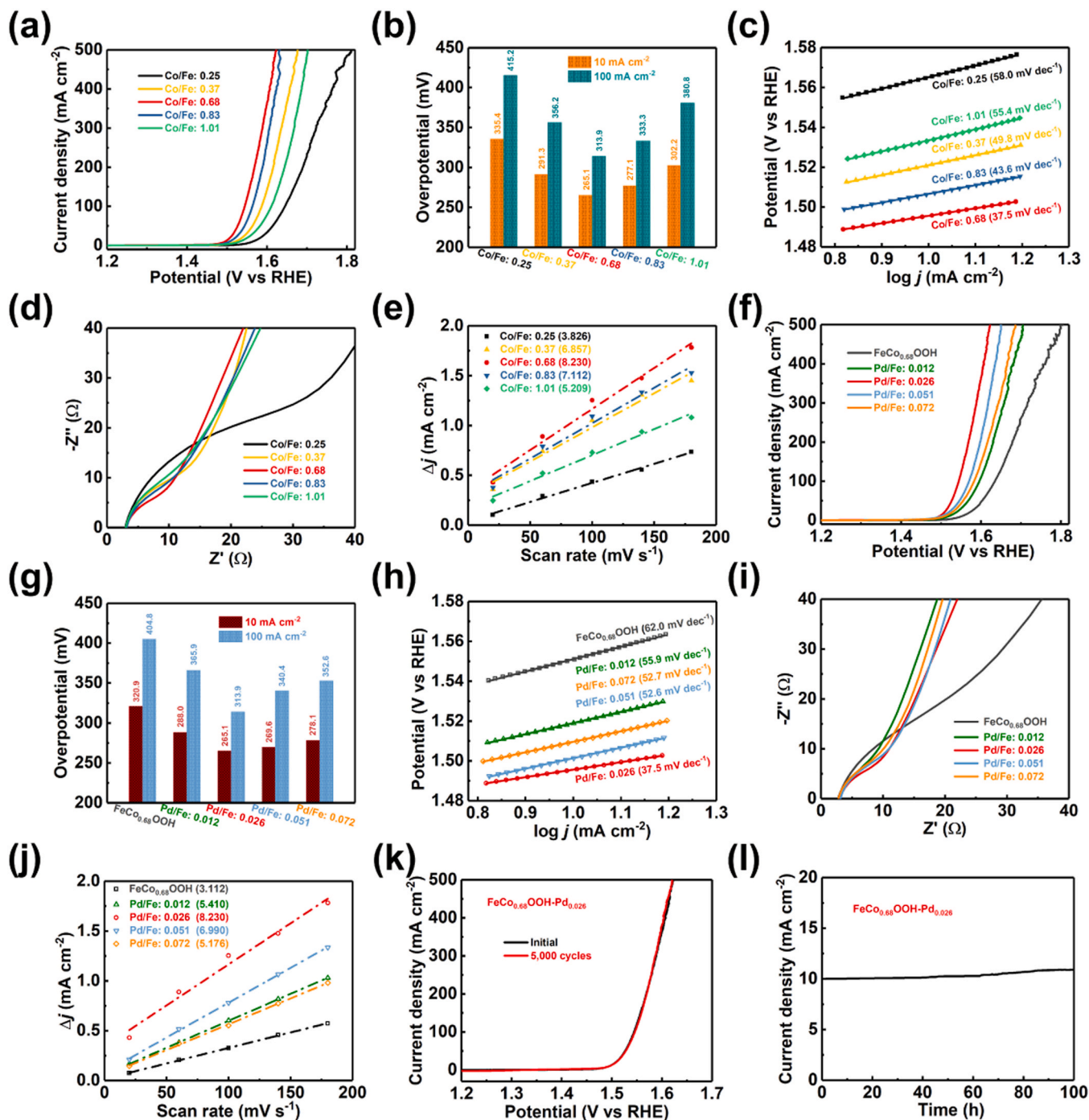
Fig. 4. (a) LSV curves, (b) the corresponding overpotentials, (c) Tafel plots, (d) EIS spectra, and (e) C_{dl} of $FeCo_aOOH-Pd_x$ in 1 M KOH. (f) LSV curves, (g) the corresponding overpotentials, (h) Tafel plots, (i) EIS spectra, and (j) C_{dl} of $FeCo_{0.68}OOH-Pd_b$ in 1 M KOH. (k) LSV curves of $FeCo_{0.68}OOH-Pd_{0.026}$ before and after 5000 cycles. (l) The current–time (i–t) chronoamperometric response of $FeCo_{0.68}OOH-Pd_{0.026}$.

evaluated by estimating the C_{dl} shown in Fig. S12. The C_{dl} order of electrocatalysts with different Co/Fe ratios is as follows: hetero-structure $FeCo_{0.68}OOH-Pd_x$ with nanorods and nanospheres coex-istence>$FeCo_{0.83}OOH-Pd_x$ with nanospheres>$FeCo_{0.37}OOH-Pd_x$ with nanorods>$FeCo_{1.01}OOH-Pd_x$ with irregular nanoparticles>$FeCo_{0.25}OOH-Pd_x$ with nanowires (Fig. 4e), demonstrating that Co doping alters the ECSA by regulating the morphology, and $FeCo_{0.68}OOH-Pd_x$ with hetero-structure exposes the most active sites in OER processes. Furthermore, the LSV curves normalized by ECSA were used to inves-tigate the effect of Co/Fe ratio on the intrinsic activity of the $FeCo_aOOH-Pd_x$ (Fig. S13a). As shown in Figs. S13b and S13c, the overpotentials and

Tafel slope of the $FeCo_{0.68}OOH-Pd_x$ are lower than those of the other samples after ECSA normalization, indicating the outstanding intrinsic activity of the $FeCo_{0.68}OOH-Pd_x$. Accordingly, the outstanding OER performance of $FeCo_{0.68}OOH-Pd_x$ can be attributed to: 1, The formations of CoOOH species and oxygen vacancies decrease the R_{ct} and enhance the conductivity of the electrocatalyst; 2. The hetero-structure formed by the coexistence of nanorods and nanospheres improves the ECSA of electrocatalyst and increases the number of exposed active sites; 3. The appropriate amount of Co doping and oxygen vacancies modulate the electronic structure of the electrocatalyst, enhancing the intrinsic ac-tivity of the electrocatalyst by increasing the activity of active sites.

The OER activity of $FeCo_{0.68}OOH-Pd_b$ electrocatalysts were tested under the same condition. Compared with $FeCo_{0.68}OOH$ without Pd components, the OER activity of the $FeCo_{0.68}OOH-Pd_b$ is more outstanding (Fig. 4f). The onset potential, overpotentials at 10 and 100 mA cm^{-2} of $FeCo_{0.68}OOH$ are 1.49 V vs RHE, 320.9 mV, and 404.8 mV, which are 0.09 V, 55.8 mV, and 90.9 mV higher than those of the $FeCo_{0.68}OOH-Pd_{0.026}$, respectively (Fig. 4g). Moreover, it can be observed from Fig. 4h that the Tafel slope for $FeCo_{0.68}OOH$ is 62.0 mV dec^{-1}, which is much higher than that of $FeCo_{0.68}OOH-Pd_{0.026}$. The acceleration of OER kinetics indicates the necessity of Pd component to enhance OER activity. It is worth noting that as the ratio of Pd/Fe increases to 0.051, the overpotentials at 10 and 100 mA cm^{-2} increase to 269.6 and 340.4 mV, and the Tafel slope increases to 52.6 mV dec^{-1}. When Pd/Fe increases to 0.072, the OER activity of $FeCo_{0.68}OOH-Pd_{0.072}$ further decreases.

The sluggish kinetics of $FeCo_{0.68}OOH-Pd_b$ with high Pd/Fe ratios are speculated to be related to the size of Pd species. Fig. S14 illustrates the effect of Pd loading on the mass activities of the electrocatalysts at an overpotential of 320 mV. For low Pd/Fe ratios (0.012, 0.026), the mass activities of the electrocatalysts are more outstanding, with the highest mass activity reaching 17.1 A mg$_{Pd}^{-1}$ at a Pd/Fe ratio of 0.026. However, as the Pd/Fe ratios increase to 0.051 and 0.072, the mass activities of the electrocatalysts decrease significantly, which are only 0.24 and 0.13 times that of $FeCo_{0.68}OOH-Pd_{0.026}$, respectively. The Pd species in $FeCo_{0.68}OOH-Pd_{0.012}$ and $FeCo_{0.68}OOH-Pd_{0.026}$ are dispersed at atomic level, and increasing the number of Pd atoms can provide more unsaturated coordination active centers. However, when the Pd content exceeds the upper limit of atomic level dispersion, the formation of Pd nanoparticles weakens the electron exchange interaction between Pd species and the support, thereby reducing the intrinsic activity of the electrocatalyst. EIS analysis explains the mechanism of OER activity enhancement. As the Nyquist plots shown in Fig. 4i, the high-frequency semicircle of $FeCo_{0.68}OOH-Pd_{0.026}$ among $FeCo_{0.68}OOH-Pd_b$ catalysts is the smallest, revealing that the R_{ct} related to electron-transfer at the electrode interface is the smallest, leading to a lower overpotential. Furthermore, C_{dl} measurements were carried out to investigate the effect of Pd species morphology on ECSA (Fig. S15). As shown in Fig. 4j, $FeCo_{0.68}OOH-Pd_{0.026}$ possesses the highest C_{dl} (8.230 mF cm^{-2}), which can be attributed to abundant unsaturated sites provided by atomic dispersed Pd species, while the formation of nanoparticles will reduce the number of active sites. The LSV curves normalized by ECSA shown in Fig. S16a demonstrate the outstanding intrinsic activity of $FeCo_{0.68}OOH-Pd_{0.026}$, revealing the significant role of unsaturated coordination centers in the formation of highly active electronic states. Compared with $FeCo_{0.68}OOH-Pd_{0.026}$, the overpotentials of $FeCo_{0.68}OOH-Pd_{0.051}$ and $FeCo_{0.68}OOH-Pd_{0.072}$ increase slightly (Fig. S16b), but the Tafel slopes increase significantly (Fig. S16c), indicating that the sluggish OER kinetics is the reason for the lower intrinsic activity of Pd nanoparticles. Therefore, the introduction of Pd species can enhance the conductivity of $FeCo_{0.68}OOH$ by accelerating the transfer of charges on the surface of electrocatalyst. Moreover, compared with Pd nanoparticles, atomic dispersed Pd species form numerous unsaturated active centers, which can increase the number of active sites, optimize the electronic structure, accelerate reaction kinetics, and thus achieve the improvements in mass activity and OER activity.

The OER performance of the $FeCo_{0.68}OOH-Pd_b$ was optimal at a Pd/Fe ratio of 0.026, therefore $FeCo_{0.68}OOH-Pd_{0.026}$ was selected for stability testing. The polarization curve of $FeCo_{0.68}OOH-Pd_{0.026}$ does not display an obvious shift after 5000 cycles of durability test, as shown in Fig. 4k. In addition, $FeCo_{0.68}OOH-Pd_{0.026}$ exhibits remarkable long-term durability (Fig. 4l). Atomic dispersed Pd species avoid the occurrence of crystal grain migration and Ostwald ripening effect due to the limitation of active sites in a narrow range [77]. Therefore, during the continuous current-time test at 1.50 V vs RHE, the current density of the $FeCo_{0.68}OOH-Pd_{0.026}$ did not decrease within 100 h. In addition,

compared with RuO_2 as benchmark material, $FeCo_{0.68}OOH-Pd_{0.026}$ exhibits a 25.3 mV decrease in overpotential at 10 mA cm^{-2} (Fig. S17a). As shown in Fig. S17b, the lower Tafel slope of $FeCo_{0.68}OOH-Pd_{0.026}$ (37.5 mV dec^{-1}) compared to RuO_2 (78.6 mV dec^{-1}) indicates faster OER kinetics. Thanks to the cheaper price and higher OER activity, $FeCo_{0.68}OOH-Pd_{0.026}$ is a promising electrocatalyst for substituting traditional benchmark materials. Considering the excellent activity of $FeCo_{0.68}OOH-Pd_{0.026}$ towards OER, we evaluated its performances in water splitting using a two-electrode cell with N_2-satruated 1 M KOH as electrolyte and commercial Pt/C as cathode (Fig. S18a). The Pt/C || $FeCo_{0.68}OOH-Pd_{0.026}$ required the cell voltages of 1.57 and 1.63 V to achieve water splitting at current densities of 10 and 100 mA cm^{-2}, respectively. In comparison, the Pt/C || RuO_2 required cell voltages of 1.61 and 1.76 V at the same current densities (Fig. S18b). In addition, in the chronopotentiometric test at a current density of 10 mA cm^{-2}, the Pt/C || $FeCo_{0.68}OOH-Pd_{0.026}$ showed negligible growth in overpotential, while the overpotential of Pt/C || RuO_2 increased by 24.3% after 20 hours (Fig. S18c). These results demonstrate that $FeCo_{0.68}OOH-Pd_{0.026}$ exhibits excellent activity and stability, indicating its potential for widespread application in water splitting.

3.3. DFT calculations

DFT calculations were conducted to investigate the mechanism of improved OER activity of $FeCo_{0.68}OOH-Pd_{0.026}$. To determine the mechanism of $FeCo_{0.68}OOH-Pd_{0.026}$ for OER, the catalytic activities of different electrocatalysts were tested in electrolytes with pH values increased from 12.5 to 14 (Fig. S19). The OER process dominated by the adsorbate evolution mechanism (AEM) undergoes 4 steps of coupled proton-electron transfer, so the OER overpotential becomes pH-independent in the RHE scale [78]. On the contrary, the lattice oxygen oxidation mechanism (LOM) generates pH-dependent OER kinetics due to the non-concerted proton-electron transfer process including lattice oxygen [78]. As shown in Fig. S20, the overpotential of RuO_2 at 10 mA cm^{-2} increases significantly with the decrease of pH, indicating the LOM dominated OER process. However, electrocatalysts with different Co/Fe and Pd/Fe ratios exhibit pH-independent OER kinetics at RHE scale, demonstrating the AEM dominated OER pathway on $FeCo_aOOH-Pd_b$. In order to uncover the effects of Co doping, oxygen vacancies, and atomic dispersed Pd species on the electronic structure, the simulation models of FeOOH, CoOOH, FeCoOOH without oxygen vacancies, FeCoOOH, and FeCoOOH-Pd were constructed, and binding models between electrocatalysts and reaction intermediates (*OH, *O, *OOH) were constructed for calculating the ΔG during OER processes (Figs. S21-S25). Fig. 5a shows the differential charge density between FeOOH and FeCoOOH without oxygen vacancies. It can be observed that a portion of Fe atoms in FeOOH were replaced by Co atoms, resulting in electron deficient states on the surface of Co atoms and causing changes in the charge distributions of nearby O and Fe atoms. Additionally, compared with the FeCoOOH without oxygen vacancies, the generation of oxygen vacancies in the FeCoOOH forms unsaturated charge deficiency centers, while causing reconstruction of the electronic structure of surrounding atoms, resulting in changes in the binding energies of Fe 2p and Co 2p in XPS results (Fig. 5b). Finally, the differential charge density between FeCoOOH-Pd and FeCoOOH shown in Fig. 5c reveals the charge exchange interaction between atomic dispersed Pd atom and the support. In FeCoOOH-Pd, a portion of electrons from Pd atom transfer to the oxyhydroxide support, forming a state of electron deletion on the Pd surface, and forming an electron accumulation center between Pd atom and the support, significantly modulating the electronic structure of the FeCoOOH surface.

The reaction pathway for OER processes and the detailed ΔG of related steps at 1.23 V vs RHE are shown in Fig. 5d. For FeOOH, the RDS is the oxidation of *O to *OOH with a ΔG of 1.60 eV. Compared to FeOOH, CoOOH has a stronger adsorption of *O and a higher energy barrier for the formation of *OH (1.54 eV) and *OOH (1.95 eV),
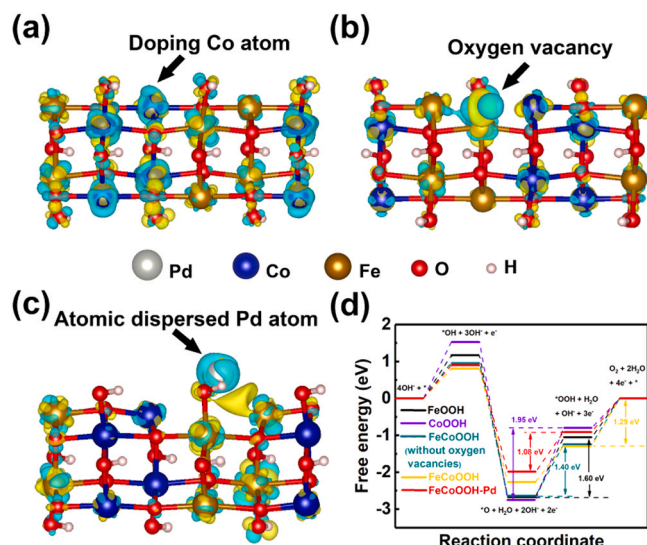
Fig. 5. Differential charge density between (a) FeOOH and FeCoOOH without oxygen vacancies, (b) FeCoOOH without oxygen vacancies and FeCoOOH, (c) FeCoOOH and FeCoOOH-Pd. The yellow and light green zones represent the charge accumulation or depletion, respectively. (d) Gibbs free energy diagram at 1.23 V for OER over different electrocatalysts.

indicating that Fe site in FeCoOOH is more favorable for OER. Benefit by the doping of Co atoms, the ΔG of the RDS in FeCoOOH without oxygen vacancies decreases to 1.40 eV. After the introduction of oxygen vacancies, the ΔG of FeCoOOH converting *O to *OOH further decreases to 0.97 eV, demonstrating the effective modulation of intermediate binding energy by oxygen vacancies. The RDS of FeCoOOH is the fourth step, and the energy barrier required for the oxidation of *OOH to O_2 is 1.29 eV. Ultimately, the atomic dispersed Pd atom further weaken the binding energy between the electrocatalyst and *O, optimize the energy required for *OOH formation, and reduce the ΔG of the RDS to 1.08 V. The RDS of FeCoOOH-Pd requires the lowest ΔG, proving that the combination of Co doping, oxygen vacancies, and atomic dispersed Pd species can modify the electronic structure on the surface of electrocatalyst and optimize the adsorption of intermediates. The calculated energy diagrams illustrate that $FeCo_{0.68}OOH-Pd_{0.026}$ exhibits the most outstanding intrinsic activity, which is beneficial for reducing the overpotential and accelerating the kinetics of OER.

4. Conclusion

In summary, amorphous hetero-structure $FeCo_{0.68}OOH-Pd_{0.026}$ was successfully fabricated via Co doping and immobilization of atomic dispersed Pd species. The $FeCo_{0.68}OOH-Pd_{0.026}$ exhibits outstanding OER performances (overpotential of 265.1 mV at 10 mA cm^{-2}, Tafel slope of 37.5 mV dec^{-1}) and outstanding stability in alkaline solution. The DFT calculation results elucidate that the modulation of charge distribution reduces the energy required for M-O oxidation to M-OOH, providing a mechanism for the accelerated kinetics of OER. Furthermore, the adjustment of electronic structure benefits from Co doping, the formation of oxygen vacancies, and the loading of atomic dispersed Pd species. Based on the analysis of experiments and characterization results, we have provided the optimal Co/Fe ratio and Pd/Fe ratio. When the Co/Fe ratio is 0.68, the formation of hetero-structure morphology and the introduction of appropriate oxygen vacancies are beneficial for exposing more active sites and improving the charge conductivity of the electrocatalyst. When Pd/Fe is 0.026, Pd atoms cannot aggregate into nanoparticles, but are dispersed at the atomic level, constructing unsaturated centers on the surface of support. The reasonably designed low-cost $FeCo_{0.68}OOH-Pd_{0.026}$ with higher electrochemical surface area and outstanding intrinsic activity overcomes

the bottlenecks of FeOOH and provides a promising electrocatalyst for large-scale application of water splitting.

Declaration of Competing Interest

The authors declare that they have no known competing financial interests or personal relationships that could have appeared to influence the work reported in this paper.

Data Availability

Data will be made available on request.

Acknowledgements

Appendix A. Supporting information

Supplementary data associated with this article can be found in the online version at doi:10.1016/j.apcatb.2024.124213.

References

[1] N.S. Lewis, Research opportunities to advance solar energy utilization, Science 351 (2016) aad1920, https://doi.org/10.1126/science.aad1920.

[2] S. Chu, Y. Cui, N. Liu, The path towards sustainable energy, Nat. Mater. 16 (2017) 16–22, https://doi.org/10.1038/nmat4834.

[3] L. Ma, Z. Wei, C. Zhao, X. Meng, H. Zhang, M. Song, Y. Wang, B. Li, X. Huang, C. Xu, M. Feng, P. He, D. Jia, Y. Zhou, X. Duan, Hierarchical superhydrophilic/ superaerophobic 3D porous trimetallic (Fe, Co, Ni) spinel/carbon/nickel foam for boosting oxygen evolution reaction, Appl. Catal. B: Environ. 332 (2023) 122717, https://doi.org/10.1016/j.apcatb.2023.122717.

[4] S. Aslam, S. Rani, K. Lal, M. Fatima, T. Hardwick, B. Shirinfar, N. Ahmed, Electrochemical hydrogen production: sustainable hydrogen economy, Green. Chem. 25 (2023) 9543–9573, https://doi.org/10.1039/D3GC02849F.

[5] A. Peugeot, C.E. Creissen, D. Karapinar, H.N. Tran, M. Schreiber, M. Fontecave, Benchmarking of oxygen evolution catalysts on porous nickel supports, Joule 5 (2021) 1281–1300, https://doi.org/10.1016/j.joule.2021.03.022.

[6] J. Zhu, L. Hu, P. Zhao, L.Y.S. Lee, K.-Y. Wong, Recent advances in electrocatalytic hydrogen evolution using nanoparticles, Chem. Rev. 120 (2020) 851–918, https://doi.org/10.1021/acs.chemrev.9b00248.

[7] S. Higashi, A. Beniya, Ultralight conductive IrO$_2$ nanostructured textile enables highly efficient hydrogen and oxygen evolution reaction: importance of catalyst layer sheet resistance, Appl. Catal. B: Environ. 321 (2023) 122030, https://doi.org/10.1016/j.apcatb.2022.122030.

[8] T. Li, O. Kasian, S. Cherevko, S. Zhang, S. Geiger, C. Scheu, P. Felfer, D. Raabe, B. Gault, K.J.J. Mayrhofer, Atomic-scale insights into surface species of electrocatalysts in three dimensions, Nat. Catal. 1 (2018) 300–305, https://doi.org/10.1038/s41929-018-0043-3.

[9] X. Xie, X. Zhang, W. Tian, X. Zhang, J. Ding, Y. Liu, S. Lu, Tri-functional Ru-RuO$_2$/ Mn-MoO$_2$ composite: a high efficient electrocatalyst for overall water splitting and rechargeable Zn–air batteries, Chem. Eng. J. 468 (2023) 143760, https://doi.org/10.1016/j.cej.2023.143760.

[10] J. Wang, H. Yang, F. Li, L. Li, J. Wu, S. Liu, T. Cheng, Y. Xu, Q. Shao, X. Huang, Single-site Pt-doped RuO$_2$ hollow nanospheres with interstitial C for high-performance acidic overall water splitting, Sci. Adv. 8 (2022) eabl9271, https://doi.org/10.1126/sciadv.abl9271.

[11] P. Zhai, M. Xia, Y. Wu, G. Zhang, J. Gao, B. Zhang, S. Cao, Y. Zhang, Z. Li, Z. Fan, C. Wang, X. Zhang, J.T. Miller, L. Sun, J. Hou, Engineering single-atomic ruthenium catalytic sites on defective nickel-iron layered double hydroxide for overall water splitting, Nat. Commun. 12 (2021) 4587, https://doi.org/10.1038/s41467-021-24828-9.

[12] L. Pan, Q. Wang, Y. Li, C. Zhang, Amorphous cobalt-cerium binary metal oxides as high performance electrocatalyst for oxygen evolution reaction, J. Catal. 384 (2020) 14–21, https://doi.org/10.1016/j.jcat.2020.02.005.

[13] J. He, T. Wu, S.-Y. Chen, R. Miao, Y. Dang, W. Zhong, M. Wang, T. Jiang, S.L. Suib, Structure-property relationship of graphene coupled metal (Ni, Co, Fe) (oxy) hydroxides for efficient electrochemical evolution of oxygen, J. Catal. 377 (2019) 619–628, https://doi.org/10.1016/j.jcat.2019.08.006.

[14] J. Du, H. Zhang, W. Hu, Z. Li, W. Gao, X. Wang, C. Li, Grain boundary effects of hierarchical Ni-Fe (oxy)hydroxide nanosheets in water oxidation, Small 19 (2023) 2304245, https://doi.org/10.1002/smll.202304245.

[15] Z. Masoumi, M. Tayebi, M. Kolaei, B.-K. Lee, Efficient and stable core-shell α–Fe$_2$O$_3$/WS$_2$/WO$_x$ photoanode for oxygen evolution reaction to enhance

photoelectrochemical water splitting, Appl. Catal. B: Environ. 313 (2022) 121447, https://doi.org/10.1016/j.apcatb.2022.121447.

[16] C. Feng, B. Zhao, Y. Bi, Constructing large-size and ultrathin NiCoP nanosheets on an Fe₂O₃ photoanode toward efficient solar water splitting, J. Mater. Chem. A 10 (2022) 12811–12816, https://doi.org/10.1039/D2TA02702J.

[17] P. Sharma, D. Mukherjee, S. Sarkar, D. Mandler, R.S. Varma, M.B. Gawande, R. Zbořil, Y. Sasson, Pd doped carbon nitride (Pd-g-C₃N₄): an efficient photocatalyst for hydrogenation via an Al–H₂O system and an electrocatalyst towards overall water splitting, Green. Chem. 24 (2022) 5535–5546, https://doi.org/10.1039/D2GC00801G.

[18] M. Benedet, G. Andrea Rizzi, A. Gasparotto, O.I. Lebedev, L. Girardi, C. Maccato, D. Barreca, Tailoring oxygen evolution performances of carbon nitride systems fabricated by electrophoresis through Ag and Au plasma functionalization, Chem. Eng. J. 448 (2022) 137645, https://doi.org/10.1016/j.cej.2022.137645.

[19] Q. Wang, M. Nakabayashi, T. Hisatomi, S. Sun, S. Akiyama, Z. Wang, Z. Pan, X. Xiao, T. Watanabe, T. Yamada, N. Shibata, T. Takata, K. Domen, Oxysulfide photocatalyst for visible-light-driven overall water splitting, Nat. Mater. 18 (2019) 827–832, https://doi.org/10.1038/s41563-019-0399-z.

[20] Y. Yang, H. Yao, Z. Yu, S.M. Islam, H. He, M. Yuan, Y. Yue, K. Xu, W. Hao, G. Sun, H. Li, S. Ma, P. Zapol, M.G. Kanatzidis, Hierarchical nanoassembly of MoS₂/Co₉S₈/Ni₃S₂/Ni as a highly efficient electrocatalyst for overall water splitting in a wide pH range, J. Am. Chem. Soc. 141 (2019) 10417–10430, https://doi.org/10.1021/jacs.9b04492.

[21] S. Yang, J.-Y. Zhu, X.-N. Chen, M.-J. Huang, S.-H. Cai, J.-Y. Han, J.-S. Li, Self-supported bimetallic phosphides with artificial heterointerfaces for enhanced electrochemical water splitting, Appl. Catal. B: Environ. 304 (2022) 120914, https://doi.org/10.1016/j.apcatb.2021.120914.

[22] R. Zhang, Z. Wei, G. Ye, G. Chen, J. Miao, X. Zhou, X. Zhu, X. Cao, X. Sun, "d-electron complementation" induced V-Co phosphide for efficient overall water splitting, Adv. Energy Mater. 11 (2021) 2101758, https://doi.org/10.1002/aenm.202101758.

[23] C. Kuai, Z. Xu, C. Xi, A. Hu, Z. Yang, Y. Zhang, C.-J. Sun, L. Li, D. Sokaras, C. Dong, S.-Z. Qiao, X.-W. Du, F. Lin, Phase segregation reversibility in mixed-metal hydroxide water oxidation catalysts, Nat. Catal. 3 (2020) 743–753, https://doi.org/10.1038/s41929-020-0496-z.

[24] S. Niu, W.-J. Jiang, Z. Wei, T. Tang, J. Ma, J.-S. Hu, L.-J. Wan, Se-doping activates FeOOH for cost-effective and efficient electrochemical water oxidation, J. Am. Chem. Soc. 141 (2019) 7005–7013, https://doi.org/10.1021/jacs.9b01214.

[25] C. Liang, P. Zou, A. Nairan, Y. Zhang, J. Liu, K. Liu, S. Hu, F. Kang, H.J. Fan, C. Yang, Exceptional performance of hierarchical Ni–Fe oxyhydroxide@NiFe alloy nanowire array electrocatalysts for large current density water splitting, Energy Environ. Sci. 13 (2020) 86–95, https://doi.org/10.1039/C9EE02388G.

[26] M. Zheng, K. Guo, W.-J. Jiang, T. Tang, X. Wang, P. Zhou, J. Du, Y. Zhao, C. Xu, J.-S. Hu, When MoS₂ meets FeOOH: a "one-stone-two-birds'' heterostructure as a bifunctional electrocatalyst for efficient alkaline water splitting, Appl. Catal. B: Environ. 244 (2019) 1004–1012, https://doi.org/10.1016/j.apcatb.2018.12.019.

[27] J. Hu, S. Zheng, X. Zhao, X. Yao, Z. Chen, A theoretical study on the surface and interfacial properties of Ni₃P for the hydrogen evolution reaction, J. Mater. Chem. A 6 (2018) 7827–7834, https://doi.org/10.1039/C8TA00437D.

[28] J. Zhang, J. Liu, L. Xi, Y. Yu, N. Chen, S. Sun, W. Wang, K.M. Lange, B. Zhang, Single-atom Au/NiFe layered double hydroxide electrocatalyst: probing the origin of activity for oxygen evolution reaction, J. Am. Chem. Soc. 140 (2018) 3876–3879, https://doi.org/10.1021/jacs.8b00752.

[29] D. Li, R. Xiang, F. Yu, J. Zeng, Y. Zhang, W. Zhou, L. Liao, Y. Zhang, D. Tang, H. Zhou, In situ regulating cobalt/iron oxide-oxyhydroxide exchange by dynamic iron incorporation for robust oxygen evolution at large current density, Adv. Mater. 36 (2024) 2305685, https://doi.org/10.1002/adma.202305685.

[30] T.W. Kim, K.-S. Choi, Nanoporous BiVO₄ photoanodes with dual-layer oxygen evolution catalysts for solar water splitting, Science 343 (2014) 990–994, https://doi.org/10.1126/science.1246913.

[31] M.B. Stevens, L.J. Enman, A.S. Batchellor, M.R. Cosby, A.E. Vise, C.D.M. Trang, S. W. Boettcher, Measurement techniques for the study of thin film heterogeneous water oxidation electrocatalysts, Chem. Mater. 29 (2017) 120–140, https://doi.org/10.1021/acs.chemmater.6b02796.

[32] T. Wang, X. Long, S. Wei, P. Wang, C. Wang, J. Jin, G. Hu, Boosting hole transfer in the fluorine-doped hematite photoanode by depositing ultrathin amorphous FeOOH/CoOOH cocatalysts, ACS Appl. Mater. Interfaces 12 (2020) 49705–49712, https://doi.org/10.1021/acsami.0c15568.

[33] Z. Wang, Z. Wang, W. Liu, W. Xiao, X.W. Lou, Amorphous CoSnO₃@C nanoboxes with superior lithium storage capability, Energy Environ. Sci. 6 (2013) 87–91, https://doi.org/10.1039/C2EE23330D.

[34] T. Guo, L. Li, Z. Wang, Recent development and future perspectives of amorphous transition metal-based electrocatalysts for oxygen evolution reaction, Adv. Energy Mater. 12 (2022) 2200827, https://doi.org/10.1002/aenm.202200827.

[35] O.B. Chae, J. Kim, I. Park, H. Jeong, J.H. Ku, J.H. Ryu, K. Kang, S.M. Oh, Reversible lithium storage at highly populated vacant sites in an amorphous vanadium pentoxide electrode, Chem. Mater. 26 (2014) 5874–5881, https://doi.org/10.1021/cm502268u.

[36] T. Guo, P. Hu, L. Li, Z. Wang, L. Guo, Amorphous materials emerging as prospective electrodes for electrochemical energy storage and conversion, Chem 9 (2023) 1080–1093, https://doi.org/10.1016/j.chempr.2023.03.032.

[37] A.J. Medford, A. Vojvodic, J.S. Hummelshøj, J. Voss, F. Abild-Pedersen, F. Studt, T. Bligaard, A. Nilsson, J.K. Nørskov, From the Sabatier principle to a predictive theory of transition-metal heterogeneous catalysis, J. Catal. 328 (2015) 36–42, https://doi.org/10.1016/j.jcat.2014.12.033.

[38] K. Zeng, W. Li, Y. Zhou, Z. Sun, C. Lu, J. Yan, J.-H. Choi, R. Yang, Multilayer hollow MnCo₂O₄ microsphere with oxygen vacancies as efficient electrocatalyst for oxygen evolution reaction, Chem. Eng. J. 421 (2021) 127831, https://doi.org/10.1016/j.cej.2020.127831.

[39] K. Chi, X. Tian, Q. Wang, Z. Zhang, X. Zhang, Y. Zhang, F. Jing, Q. Lv, W. Yao, F. Xiao, S. Wang, Oxygen vacancies engineered CoMoO₄ nanosheet arrays as efficient bifunctional electrocatalysts for overall water splitting, J. Catal. 381 (2020) 44–52, https://doi.org/10.1016/j.jcat.2019.10.025.

[40] K. Zhu, T. Wu, M. Li, R. Lu, X. Zhu, W. Yang, Perovskites decorated with oxygen vacancies and Fe–Ni alloy nanoparticles as high-efficiency electrocatalysts for the oxygen evolution reaction, J. Mater. Chem. A 5 (2017) 19836–19845, https://doi.org/10.1039/C7TA05404A.

[41] W.T. Hong, M. Risch, K.A. Stoerzinger, A. Grimaud, J. Suntivich, Y. Shao-Horn, Toward the rational design of non-precious transition metal oxides for oxygen electrocatalysis, Energy Environ. Sci. 8 (2015) 1404–1427, https://doi.org/10.1039/C4EE03869J.

[42] D. Yan, Y. Li, J. Huo, R. Chen, L. Dai, S. Wang, Defect chemistry of nonprecious-metal electrocatalysts for oxygen reactions, Adv. Mater. 29 (2017) 1606459, https://doi.org/10.1002/adma.201606459.

[43] H.B. Tao, L. Fang, J. Chen, H.B. Yang, J. Gao, J. Miao, S. Chen, B. Liu, Identification of surface reactivity descriptor for transition metal oxides in oxygen evolution reaction, J. Am. Chem. Soc. 138 (2016) 9978–9985, https://doi.org/10.1021/jacs.6b05398.

[44] J. Zheng, W. Zhang, R. Wang, J. Wang, Y. Zhai, X. Liu, Single-atom Pd-N₄ catalysis for stable low-overpotential lithium-oxygen battery, Small 19 (2023) 2204559, https://doi.org/10.1002/smll.202204559.

[45] W. Xiang, Y. Zhao, Z. Jiang, X. Li, H. Zhang, Y. Sun, Z. Ning, F. Du, P. Gao, J. Qian, K. Kato, M. Yamauchi, Y. Sun, Palladium single atoms supported by interwoven carbon nanotube and manganese oxide nanowire networks for enhanced electrocatalysis, J. Mater. Chem. A 6 (2018) 23366–23377, https://doi.org/10.1039/C8TA09034C.

[46] J. Li, L.-W. Chen, Y.-C. Hao, M. Yuan, J. Lv, A. Dong, S. Li, H. Gu, A.-X. Yin, W. Chen, P. Li, B. Wang, Asymmetric coordinated single-atom Pd sites for high performance CO₂ electroreduction and Zn–CO₂ battery, Chem. Eng. J. 461 (2023) 141865, https://doi.org/10.1016/j.cej.2023.141865.

[47] T.D. Kühne, M. Iannuzzi, M. Del Ben, V.V. Rybkin, P. Seewald, F. Stein, T. Laino, R. Z. Khaliullin, O. Schütt, F. Schiffmann, D. Golze, J. Wilhelm, S. Chulkov, M. H. Bani-Hashemian, V. Weber, U. Borštnik, M. Taillefumier, A.S. Jakobovits, A. Lazzaro, H. Pabst, T. Müller, R. Schade, M. Guidon, S. Andermatt, N. Holmberg, G.K. Schenter, A. Hehn, A. Bussy, F. Belleflamme, G. Tabacchi, A. Glöß, M. Lass, I. Bethune, C.J. Mundy, M. Watkins, J. VandeVondele, M. Krack, J. Hutter, CP2K: an electronic structure and molecular dynamics software package-quickstep: efficient and accurate electronic structure calculations, J. Chem. Phys. 152 (2020) 194103, https://doi.org/10.1063/5.0007045.

[48] S. Goedecker, M. Teter, J. Hutter, Separable dual-space Gaussian pseudopotentials, Phys. Rev. B 54 (1996) 1703–1710, https://doi.org/10.1103/PhysRevB.54.1703.

[49] M. Guidon, J. Hutter, J. VandeVondele, Auxiliary density matrix methods for Hartree-Fock exchange calculations, J. Chem. Theory Comput. 6 (2010) 2348–2364, https://doi.org/10.1021/ct1002225.

[50] A. Hellman, R.G.S. Pala, First-principles study of photoinduced water-splitting on Fe₂O₃, J. Phys. Chem. C. 115 (2011) 12901–12907, https://doi.org/10.1021/jp200751j.

[51] J. VandeVondele, J. Hutter, Gaussian basis sets for accurate calculations on molecular systems in gas and condensed phases, J. Chem. Phys. 127 (2007) 114105, https://doi.org/10.1063/1.2770708.

[52] S. Niu, R. McFeron, F. Godínez-Salomón, B.S. Chapman, C.A. Damin, J.B. Tracy, V. Augustyn, C.P. Rhodes, Enhanced electrochemical lithium-ion charge storage of iron oxide nanosheets, Chem. Mater. 29 (2017) 7794–7807, https://doi.org/10.1021/acs.chemmater.7b02315.

[53] W. Chen, Y. Ma, F. Li, L. Pan, W. Gao, Q. Xiang, W. Shang, C. Song, P. Tao, H. Zhu, X. Pan, T. Deng, J. Wu, Strong electronic interaction of amorphous Fe₂O₃ nanosheets with single-atom Pt toward enhanced carbon monoxide oxidation, Adv. Funct. Mater. 29 (2019) 1904278, https://doi.org/10.1002/adfm.201904278.

[54] B. Wei, C. Shang, X. Wang, G. Zhou, Conductive FeOOH as multifunctional interlayer for superior lithium–sulfur batteries, Small 16 (2020) 2002789, https://doi.org/10.1002/smll.202002789.

[55] Q. Liu, Q. Liu, L. Xie, Y. Ji, T. Li, B. Zhang, N. Li, B. Tang, Y. Liu, S. Gao, Y. Luo, L. Yu, Q. Kong, X. Sun, High-performance electrochemical nitrate reduction to ammonia under ambient conditions using a FeOOH nanorod catalyst, Appl. Mater. Interfaces 14 (2022) 17312–17318, https://doi.org/10.1021/acsami.2c00436.

[56] S.-H. Ye, Z.-X. Shi, J.-X. Feng, Y.-X. Tong, G.-R. Li, Activating CoOOH porous nanosheet arrays by partial iron substitution for efficient oxygen evolution reaction, Angew. Chem. Int. Ed. 57 (2018) 2672–2676, https://doi.org/10.1002/anie.201712549.

[57] J. Li, M.-X. Guan, P.-F. Nan, J. Wang, B.-H. Ge, K.-M. Qiao, H.-R. Zhang, W.-H. Liang, J.-Z. Hao, H.-B. Zhou, F.-R. Shen, F.-X. Liang, C. Zhang, M. Liu, S. Meng, T. Zhu, F.-X. Hu, T. Wu, J.-D. Guo, J.-R. Sun, B.-G. Shen, Topotactic phase transformations by concerted dual-ion migration of B-site cation and oxygen in multivalent cobaltite La–Sr–Co–Ox films, Nano Energy 78 (2020) 105215, https://doi.org/10.1016/j.nanoen.2020.105215.

[58] S.B. Kulkarni, V.S. Jamadade, D.S. Dhawale, C.D. Lokhande, Synthesis and characterization of β-Ni(OH)₂ up grown nanoflakes by SILAR method, Appl. Surf. Sci. 255 (2009) 8390–8394, https://doi.org/10.1016/j.apsusc.2009.05.095.

[59] H. Antony, S. Peulon, L. Legrand, A. Chaussé, Electrochemical synthesis of lepidocrocite thin films on gold substrate—EQCM, IRRAS, SEM and XRD study,

Electrochim. Acta 50 (2004) 1015–1021, https://doi.org/10.1016/j. electacta.2004.07.043.

[60] S.-H. Wen, X.-L. Zhong, Y.-D. Wu, R.-P. Liang, L. Zhang, J.-D. Qiu, Colorimetric assay conversion to highly sensitive electrochemical assay for bimodal detection of arsenate based on cobalt oxyhydroxide nanozyme via arsenate absorption, Anal. Chem. 91 (2019) 6487–6497, https://doi.org/10.1021/acs.analchem.8b05121.

[61] F. Geng, Z. Zhao, J. Geng, H. Cong, H.-M. Cheng, A simple and low-temperature hydrothermal route for the synthesis of tubular α-FeOOH, Mater. Lett. 61 (2007) 4794–4796, https://doi.org/10.1016/j.matlet.2007.03.036.

[62] C. Manjunatha, N. Srinivasa, S. Samriddhi, C. Vidya, S. Ashoka, Studies on anion-induced structural transformations of iron(III) (hydr)oxide micro-nanostructures and their oxygen evolution reaction performance, Solid State Sci. 106 (2020) 106314, https://doi.org/10.1016/j.solidstatesciences.2020.106314.

[63] M. Yang, Y.-X. Li, M. Jiang, P.-H. Li, S.-H. Chen, J.-H. Liu, C.-H. Lin, X.-J. Huang, W.-Q. Liu, Identifying phase-dependent electrochemical stripping performance of FeOOH nanorod: evidence from kinetic simulation and analyte–material interactions, Small 16 (2020) 1906830, https://doi.org/10.1002/smll.201906830.

[64] X. Zhang, Y. Liu, S. Dong, Z. Ye, Y. Wei, Low-temperature synthesized nanocomposites with amorphous FeOOH on $Ti_3C_2T_x$ for supercapacitors, J. Alloy. Compd. 744 (2018) 507–515, https://doi.org/10.1016/j.jallcom.2018.02.080.

[65] Y. Ai, L. Liu, C. Zhang, L. Qi, M. He, Z. Liang, H.-b Sun, G. Luo, Q. Liang, Amorphous flowerlike goethite FeOOH hierarchical supraparticles: superior capability for catalytic hydrogenation of nitroaromatics in water, ACS Appl. Mater. Interfaces 10 (2018) 32180–32191, https://doi.org/10.1021/acsami.8b10711.

[66] J. Lv, X. Guan, Y. Huang, L. Cai, M. Yu, X. Li, Y. Yu, D. Chen, Stepwise chemical oxidation to access ultrathin metal (oxy)-hydroxide nanosheets for the oxygen evolution reaction, Nanoscale 13 (2021) 15755–15762, https://doi.org/10.1039/D1NR03813C.

[67] M.S. Burke, M.G. Kast, L. Trotochaud, A.M. Smith, S.W. Boettcher, Cobalt–iron (oxy)hydroxide oxygen evolution electrocatalysts: the role of structure and composition on activity, stability, and mechanism, J. Am. Chem. Soc. 137 (2015) 3638–3648, https://doi.org/10.1021/jacs.5b00281.

[68] W.-G. Lim, C. Jo, A. Cho, J. Hwang, S. Kim, J.W. Han, J. Lee, Approaching ultrastable high-rate Li–S batteries through hierarchically porous titanium nitride synthesized by multiscale phase separation, Adv. Mater. 31 (2019) 1806547, https://doi.org/10.1002/adma.201806547.

[69] R.-N. Luan, N. Xu, C.-R. Li, Z.-J. Zhang, Y.-S. Zhang, J. Nan, S.-T. Wang, Y.-M. Chai, B. Dong, Engineering heterogeneous synergistic interface and multifunctional cobalt-iron site enabling high-performance oxygen evolution reaction, J. Alloy. Compd. 972 (2024) 172763, https://doi.org/10.1016/j.jallcom.2023.172763.

[70] B. Zhang, L. Wang, Y. Zhang, Y. Ding, Y. Bi, Ultrathin FeOOH nanolayers with abundant oxygen vacancies on $BiVO_4$ photoanodes for efficient water oxidation, Angew. Chem. Int. Ed. 57 (2018) 2248–2252, https://doi.org/10.1002/anie.201712499.

[71] D.C. Connors, R.N. West, Positron annihilation and defects in metals, Phys. Lett. A 30 (1969) 24–25, https://doi.org/10.1016/0375-9601(69)90018-8.

[72] X. Liu, K. Zhou, L. Wang, B. Wang, Y. Li, Oxygen vacancy clusters promoting reducibility and activity of ceria nanorods, J. Am. Chem. Soc. 131 (2009) 3140–3141, https://doi.org/10.1021/ja808433d.

[73] X. Jiang, Y. Zhang, J. Jiang, Y. Rong, Y. Wang, Y. Wu, C. Pan, Characterization of oxygen vacancy associates within hydrogenated TiO_2: a positron annihilation study, J. Phys. Chem. C. 116 (2012) 22619–22624, https://doi.org/10.1021/jp307573c.

[74] S. Yang, Z. Si, G. Li, P. Zhan, C. Liu, L. Lu, B. Han, H. Xie, P. Qin, Single cobalt atoms immobilized on palladium-based nanosheets as 2D single-atom alloy for efficient hydrogen evolution reaction, Small 19 (2023) 2207651, https://doi.org/10.1002/smll.202207651.

[75] R. Lang, X. Du, Y. Huang, X. Jiang, Q. Zhang, Y. Guo, K. Liu, B. Qiao, A. Wang, T. Zhang, Single-atom catalysts based on the metal-oxide interaction, Chem. Rev. 120 (2020) 11986–12043, https://doi.org/10.1021/acs.chemrev.0c00797.

[76] P. Qin, S. Yang, P. Zhan, M. Chu, G. Li, Z. Si, J. Shi, L. Lu, B. Han, T. Tan, Two-dimensional PdMo curved nanosheets for tunable CO_2 electrocatalytic reduction to syngas, Cell Rep. Phys. Sci. 2 (2021) 100619, https://doi.org/10.1016/j.xcrp.2021.100619.

[77] K. Wettergren, F.F. Schweinberger, D. Deiana, C.J. Ridge, A.S. Crampton, M. D. Rötzer, T.W. Hansen, V.P. Zhdanov, U. Heiz, C. Langhammer, High sintering resistance of size-selected platinum cluster catalysts by suppressed Ostwald ripening, Nano Lett. 14 (2014) 5803–5809, https://doi.org/10.1021/nl502686u.

[78] M. Chatenet, B.G. Pollet, D.R. Dekel, F. Dionigi, J. Deseure, P. Millet, R.D. Braatz, M.Z. Bazant, M. Eikerling, I. Staffell, P. Balcombe, Y. Shao-Horn, H. Schäfer, Water electrolysis: from textbook knowledge to the latest scientific strategies and industrial developments, Chem. Soc. Rev. 51 (2022) 4583–4762, https://doi.org/10.1039/D0CS01079K.